Structural Model Decomposition-Based Distributed Monitoring for Early Instability Detection in Inverter-Dominated Microgrids

1st Fatemeh Nasr Esfahani
School of Engineering
Lancaster University
Lancaster, UK
f.nasresfahani@lancaster.ac.uk

2nd Neeraj Suri
School of Computing and Communications
Lancaster University
Lancaster, UK
neeraj.suri@lancaster.ac.uk

3rd Yueqi Wu
TNEI Group
Manchester, UK
yueqi.wu@tneigroup.com

4th Mohamed Galeela
TNEI Group
Manchester, UK
mohamed.galeela@tneigroup.com

5th Xiandong Ma*
School of Engineering
Lancaster University
Lancaster, UK
xiandong.ma@lancaster.ac.uk

***Abstract*—The increasing penetration of inverter-based resources (IBRs) is driving power systems toward inverter-dominated operation, where reduced inertia and stronger inter-device coupling require improved real-time monitoring. This paper presents a distributed monitoring framework for inverter-dominated microgrids based on structural model decomposition (SMD). The network is decomposed into interacting subsystems connected through explicit boundary variables, from which measurable residual signals are constructed. A normalised residual energy metric combined with a gated cumulative sum (CUSUM) detector is used to identify sustained structural inconsistencies using only boundary measurements, without observer design or internal state reconstruction. The method is evaluated under benign load disturbances and droop-law parameter modifications in a three-inverter islanded microgrid. Simulation results show that the proposed framework distinguishes normal transient behaviour from structural regime changes and provides early awareness of altered inter-inverter coupling before large voltage deviations occur.**

***Index Terms*—Anomaly Detection, Distributed Monitoring, Inverter-Based Resources, Microgrids, Stability Awareness, Structural Model Decomposition**

I. Introduction

The rapid growth of inverter-based resources (IBRs) is transforming power systems into distributed, tightly coupled networks with reduced inertia and faster dynamics [1]. In islanded or weak-grid conditions, reduced damping and strong coupling increase disturbance sensitivity [2]. As inverter penetration grows, real-time awareness of coupling behaviour and emerging instability becomes essential [3]. Increasing converter interactions and distributed control layers further complicate real-time monitoring and stability assessment in modern power systems [4], [5].

A substantial body of research addresses stability and coordination in IBRs [6], [7]. Control-oriented studies focus on droop tuning, virtual synchronous generator design, hierarchical regulation, and small-signal stability analysis to enhance damping and power sharing [8], [9]. Optimisation-based approaches employ distributed algorithms to coordinate active and reactive power under operational constraints [10], [11]. Although these methods are essential for improving regulation and robustness, they are primarily formulated for controller synthesis and performance optimisation under assumed operating conditions. They are not designed to provide scalable, distributed monitoring of structural interactions between subsystems or to detect persistent violations of interconnection constraints in real time. Besides, many anomaly detection and instability awareness approaches rely on aggregated measurements, phasor data, or data-driven models [12]–[14]. Although effective for event classification or disturbance identification, they typically do not directly exploit the physical coupling constraints (e.g., voltage continuity and current balance) governing inter-inverter interaction at network interfaces. As a result, structural inconsistencies at subsystem boundaries may not be clearly isolated or or interpreted.

This reveals a research gap. Although monitoring and anomaly detection methods exist for inverter-dominated systems, limited attention has been given to frameworks that explicitly track interface consistency between inverter subsystems in a distributed and interpretable manner. Few works formulate inter-inverter coupling constraints as measurable residuals for online persistence-based detection. In inverter-dominated microgrids, system behaviour is governed by boundary interactions at the point of common coupling (PCC) [15]. Voltage continuity and current balance define the coupling manifold between parallel inverters, and persistent deviation from these constraints reflects altered coupling, reduced damping, or control changes. Monitoring boundary relations therefore provides a direct indicator of structural consistency.

Corresponding author: Xiandong Ma (xiandong.ma@lancaster.ac.uk)

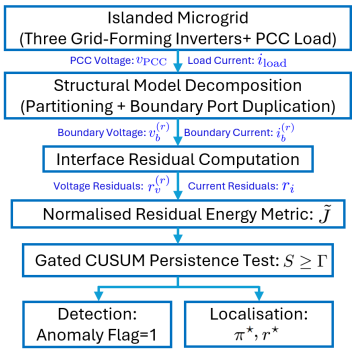

Fig. 1. Proposed SMD-based residual monitoring framework ($\pi^\star$: dominant contribution value $r^\star$: dominant inverter region).

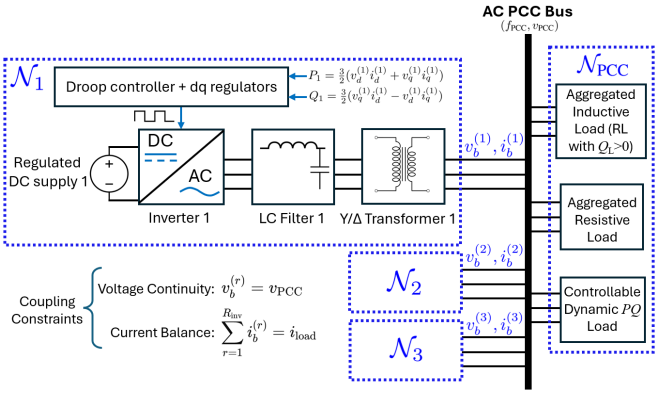

Fig. 2. Monitoring-oriented structural decomposition of the islanded inverter-based microgrid.

Structural model decomposition (SMD) offers a natural representation for this purpose. By separating internal regional dynamics from interconnection constraints, SMD reformulates the microgrid into subsystems coupled through explicit boundary port variables. SMD has primarily been employed for decomposition-based analysis, optimisation, and parallel computation in power systems [16], [17]. However, explicit formulation of boundary consistency constraints as measurable residuals for distributed monitoring in inverter-dominated microgrids has received relatively limited attention. This structural separation makes inter-inverter interaction measurable through interface quantities and provides a principled basis for distributed monitoring.

This paper proposes a distributed monitoring framework for inverter-dominated microgrids based on SMD. With a fixed inverter-level partition, PCC boundary variables are monitored directly and interface consistency constraints are converted into measurable residuals. A normalised residual energy metric combined with a gated cumulative sum (CUSUM) test detects sustained structural inconsistencies in inter-inverter coupling. The framework is evaluated on a nonlinear three-inverter islanded microgrid under load disturbances and droop-law modifications. Results show that the method distinguishes transient variations from structural regime changes and enables inverter-level localisation. Fig. 1 summarises the approach: SMD exposes boundary variables, residuals are formed from interface inconsistencies, and a persistence-based test declares detection. Localisation is achieved using per-inverter contribution scores computed from regional residual energies. Unlike conventional residual-based monitoring methods that rely on observers, global state estimation, or aggregated measurements, the proposed framework constructs residuals directly from SMD-based boundary consistency constraints at inverter interfaces. This enables distributed monitoring of inter-inverter coupling using only local boundary measurements, without full-system reconstruction or data-driven training.

The remainder of this paper is organised as follows. Section II presents the islanded microgrid model and its monitoring-oriented partitioning. Section III describes the SMD and boundary-variable formulation. Section IV defines the residual signals, energy metric, and detection logic. Section V provides a small-signal interpretation linking residual growth to stability margin reduction. Section VI presents the simulation setup and detection results. Finally, Section VII concludes the paper.

II. Microgrid Model and Monitoring-Oriented Partitioning

Before applying SMD, a fixed partition of the inverter-based microgrid is defined to identify electrical interfaces consistent with the control structure and available measurements. The partition is selected according to the microgrid interconnection structure, PCC measurement accessibility, and the requirement that inter-regional interactions occur through well-defined electrical interfaces. Since parallel inverters exchange power only through the PCC, inverter-level partitioning isolates local dynamics and preserves the dominant coupling pathways relevant for monitoring.

As shown in Fig. 2, the islanded inverter-based microgrid consists of $R_{\mathrm{inv}} = 3$ parallel grid-forming inverters connected to a common PCC supplying aggregated loads. Since inverters interact only through the PCC, the natural partition is at the inverter level. Each region $\{\mathcal{N}_r\}_{r=1}^{R_{\mathrm{inv}}}$ includes the converter, LC filter, transformer interface, and associated droop and inner control loops. Droop control provides primary frequency and voltage regulation as functions of active and reactive power, and the inner loops are fast dq-frame current and voltage regulators that track references and stabilise the converter. The DC sources are modelled as regulated supplies representing generic inverter-based resources (e.g., photovoltaic, wind, or energy storage). The PCC and connected loads form a separate region, $\mathcal{N}_{\mathrm{PCC}}$. The PCC is the sole coupling interface, and inter-regional interaction occurs only through boundary voltage and current variables. Coupling instabilities, including desynchronisation, low-frequency oscillations, and power-sharing imbalance, are reflected at the PCC interface, making the partition well suited for boundary-based monitoring.

III. Structural Model Decomposition

Given the fixed inverter-level partition, SMD rewrites the interconnected microgrid into regional subsystems coupled

exclusively through explicit boundary port variables at the PCC. The decomposition preserves physical equivalence and exposes the interfaces that govern inter-regional interaction.

Prior to decomposition, the islanded microgrid can be written in compact differential-algebraic form as below:

$$\dot{x} = f(x, z), \qquad 0 = g(x, z), \tag{1}$$

where x collects dynamic states and z algebraic network variables. The algebraic equations enforce voltage continuity and current balance at the PCC.

For each inverter region $r \in \{1, \ldots, R_{\text{inv}}\}$, boundary voltage and current port variables are defined as $v_b^{(r)}(t)$, $i_b^{(r)}(t) \in \mathbb{R}^{m_b}$, representing the inverter terminal quantities at the PCC. Here, m_b denotes the number of boundary voltage/current channels at the PCC interface (e.g., $m_b = 3$ for a three-phase representation or $m_b = 2$ in a synchronous dq frame). Each region maintains a local copy of these variables, allowing internal dynamics to be represented independently before enforcing interface consistency.

In the single-bus configuration shown in Fig. 2, all inverter regions share a common PCC voltage $v_{\text{PCC}}(t)$, and Kirchhoff's current law (KCL) relates inverter injections to the load current $i_{\text{load}}(t)$. The coupling constraints are therefore:

$$v_b^{(r)} = v_{\text{PCC}}, \qquad \sum_{r=1}^{R_{\text{inv}}} i_b^{(r)} = i_{\text{load}}. \tag{2}$$

The first constraint enforces voltage continuity at the PCC and the second enforces current balance. Boundary voltage and current variables are selected because they characterise electrical coupling through Kirchhoff's laws and directly reflect synchronisation, power-sharing, and interconnection consistency between inverter regions. Violations indicate departure from nominal coupling behaviour (e.g., desynchronisation, structural changes in the control law, or load disturbances). Other quantities, including active/reactive power and frequency estimates, are derived from these electrical variables and are therefore treated as auxiliary monitoring signals rather than independent coupling states.

Each inverter region r is described by nonlinear differential-algebraic equations of the form:

$$\begin{bmatrix} \dot{x}_r \\ 0 \\ i_b^{(r)} \end{bmatrix} = \begin{bmatrix} f_r(x_r, z_r, u_r, v_b^{(r)}) \\ g_r(x_r, z_r, u_r, v_b^{(r)}) \\ h_r(x_r, z_r, u_r, v_b^{(r)}) \end{bmatrix}. \tag{3}$$

where x_r is the dynamic state vector of region r. It includes droop control states, voltage and current regulation states in the synchronous dq frame, and the electrical states of the output filter. z_r collects algebraic variables and u_r represents local control inputs. The boundary voltage $v_b^{(r)}$ acts as an external input from the PCC, and the boundary current $i_b^{(r)}$ is the corresponding output injected into the interface. Power measurements and frequency estimates are used internally within $f_r(\cdot)$ and are not exchanged across regions. Inter-regional interaction occurs only through the boundary port variables. Each region exposes a compact measurement vector:

$$y_r = \left[v_b^{(r)},\ i_b^{(r)},\ P_r,\ Q_r,\ \hat{\omega}_r \right]^\top, \tag{4}$$

where $\hat{\omega}_r$ denotes the local frequency estimate provided by the droop controller. Although the structural formulation is coordinate-independent, the boundary variables are implemented in a synchronous dq reference frame, with $v_b^{(r)} = [\, v_d^{(r)},\, v_q^{(r)} \,]^\top$ and $i_b^{(r)} = [\, i_d^{(r)},\, i_q^{(r)} \,]^\top$, consistent with the inverter control structure.

All quantities are expressed in a common PCC-synchronous frame defined by θ_{PCC}, ensuring that boundary variables are directly comparable across regions. Notably, the full internal state vector remains local to each region, and monitoring relies only on boundary and measurable subsystem signals.

IV. Monitoring Signals and Anomaly Indicators

In droop-controlled parallel inverters, synchronisation and proportional power sharing enforce boundary consistency at the PCC. Monitoring signals are therefore derived directly from violations of the coupling constraints in (2). For each inverter region r, the voltage residual is defined as:

$$r_v^{(r)}(t) = v_b^{(r)}(t) - v_{\text{PCC}}(t) \xrightarrow{\text{dq frame}} \begin{bmatrix} v_d^{(r)} - v_d^{\text{PCC}} \\ v_q^{(r)} - v_q^{\text{PCC}} \end{bmatrix}, \tag{5}$$

which quantifies deviation from voltage continuity at the PCC. The residual is computed from independently measured or locally estimated boundary phasors. Although voltage continuity holds at an ideal bus, measurement filtering, estimation dynamics, and reference-frame mismatch render $r_v^{(r)}(t)$ nonzero under desynchronisation, bias, control-induced mismatch, or emerging instability.

Similarly, the aggregate current residual enforcing KCL is:

$$r_i(t) = \sum_{r=1}^{R_{\text{inv}}} i_b^{(r)}(t) - i_{\text{load}}(t) \xrightarrow{\text{dq frame}} r_{i,dq}(t) = \sum_{r=1}^{R_{\text{inv}}} \begin{bmatrix} i_d^{(r)} \\ i_q^{(r)} \end{bmatrix} - \begin{bmatrix} i_d^{\text{load}} \\ i_q^{\text{load}} \end{bmatrix}. \tag{6}$$

The residuals $r_v^{(r)}$ and r_i represent measurable constraint violations. Under nominal conditions, the system evolves close to the coupling manifold (2), and residual magnitudes remain bounded by measurement noise. Sustained growth indicates departure from structural consistency. In the case study, $i_{\text{load}}(t)$ is obtained from PCC measurements or the load model. In practice, it may be replaced by a direct net PCC current measurement $i_{\text{PCC}}(t)$, if available.

A normalised windowed residual energy metric is defined:

$$\tilde{J}(t) = \frac{1}{T} \int_{t-T}^{t} \left(\alpha \sum_{r=1}^{R_{\text{inv}}} \left\| \frac{r_v^{(r)}(\tau)}{V_{\text{nom}}} \right\|_2^2 + \beta \left\| \frac{r_i(\tau)}{I_{\text{nom}}} \right\|_2^2 \right) d\tau, \tag{7}$$

where T is the monitoring window, V_{nom} and I_{nom} are scalar nominal amplitudes corresponding to the rated PCC voltage and inverter current magnitudes in the selected dq reference frame. The weighting factors $\alpha, \beta > 0$ tune the relative sensitivity to voltage-consistency versus current-balance violations. Larger α increases sensitivity to desynchronisation, whereas larger β emphasises current imbalance.

Under nominal operation, the system remains in a neighbourhood of the coupling constraints in (2), and $\tilde{J}(t)$ stays small, limited mainly by measurement noise and short transient effects. Brief load changes may cause temporary increases in $\tilde{J}(t)$, but the value returns to normal once synchronisation and power sharing are re-established. In contrast, sustained

Algorithm 1 Online computation of normalised SMD residual indicator, persistence detection, localisation, and contribution score

Require: Window length T, sampling time Δt, weights $\alpha, \beta > 0$, nominal scales $V_{\mathrm{nom}}, I_{\mathrm{nom}}$, baseline statistics μ_0, σ_0, threshold factor $\eta > 0$, CUSUM parameters $\kappa > 0, \Gamma > 0$, small $\varepsilon > 0$

Compute window length in samples $N_T \leftarrow \lceil T/\Delta t \rceil$
Set instantaneous threshold $\gamma \leftarrow \mu_0 + \eta\sigma_0$
Initialise $\tilde{J}[0] \leftarrow 0$, $S[0] \leftarrow 0$, Flag $\leftarrow 0$
for $k = 1, 2, \ldots$ (each sampling instant) **do**
  Acquire PCC measurements $v_{\mathrm{PCC}}[k]$, $i_{\mathrm{load}}[k]$
  for $r = 1, \ldots, R_{\mathrm{inv}}$ **do**
    Acquire inverter boundary signals $v_b^{(r)}[k]$, $i_b^{(r)}[k]$
    Voltage residual: $r_v^{(r)}[k] \leftarrow v_b^{(r)}[k] - v_{\mathrm{PCC}}[k]$
    Normalise: $r_{v,n}^{(r)}[k] \leftarrow r_v^{(r)}[k]/V_{\mathrm{nom}}$
  end for
  Aggregate current residual (KCL): $r_i[k] \leftarrow \sum_{r=1}^{R_{\mathrm{inv}}} i_b^{(r)}[k] - i_{\mathrm{load}}[k]$
  Normalise: $r_{i,n}[k] \leftarrow r_i[k]/I_{\mathrm{nom}}$
  Instantaneous normalised residual energy: $e[k] \leftarrow \alpha \sum_{r=1}^{R_{\mathrm{inv}}} \|r_{v,n}^{(r)}[k]\|_2^2 + \beta \|r_{i,n}[k]\|_2^2$
  Update windowed indicator (sliding-window Riemann sum)
  if $k \le N_T$ **then**
    $\tilde{J}[k] \leftarrow \tilde{J}[k-1] + \dfrac{\Delta t}{T}\, e[k]$
  else
    $\tilde{J}[k] \leftarrow \tilde{J}[k-1] + \dfrac{\Delta t}{T}\, e[k] - \dfrac{\Delta t}{T}\, e[k - N_T]$
  end if
  Update persistence statistic (gated CUSUM)
  $g[k] \leftarrow \max\{0,\ \tilde{J}[k] - \gamma\}$
  $S[k] \leftarrow \max\{0,\ S[k-1] + g[k] - \kappa\}$
  if $S[k] \ge \Gamma$ **then**
    Flag $\leftarrow 1$ ▷ Anomaly/early-instability detected
    for $r = 1, \ldots, R_{\mathrm{inv}}$ **do**
      Update per-inverter energy (sliding window):
      $J_v^{(r)}[k] \leftarrow J_v^{(r)}[k-1] + \dfrac{\Delta t}{T}\|r_{v,n}^{(r)}[k]\|_2^2 - \dfrac{\Delta t}{T}\|r_{v,n}^{(r)}[k-N_T]\|_2^2$
    end for
    for $r = 1, \ldots, R_{\mathrm{inv}}$ **do**
      Contribution score: $\pi_r[k] \leftarrow \dfrac{J_v^{(r)}[k]}{\sum_{\ell=1}^{R_{\mathrm{inv}}} J_v^{(\ell)}[k] + \varepsilon}$
    end for
  else
    Flag $\leftarrow 0$
  end if
end for

structural changes in control or measurement (e.g., droop-law mis-tuning, loss of synchronisation, etc.) would lead to continued violations of the coupling constraints and persistent growth of $\tilde{J}(t)$. The metric therefore reflects the degree of departure from structural consistency at the PCC interface.

The practical implementation is summarised in Algorithm 1. At each sampling instant, boundary measurements are used to compute voltage and current residuals, which are aggregated into the discrete-time indicator $\tilde{J}[k]$ using a sliding-window sum approximating (7). A preliminary anomaly indication is obtained when $\tilde{J}[k]$ exceeds a threshold $\gamma = \mu_0 + \eta\sigma_0$, where μ_0 and σ_0 are the mean and standard deviation under nominal operation. The final decision is based on a persistence statistic to suppress short-lived excursions.

To suppress short-lived excursions, a one-sided gated CUSUM statistic is introduced. Exceedances above the threshold are defined as $g[k] = \max\{0,\ \tilde{J}[k] - \gamma\}$ and the statistic is updated as $S[k] = \max\{0,\ S[k-1] + g[k] - \kappa\}$, where $S[0] = 0$ and $\kappa > 0$ controls sensitivity. An anomaly is declared when $S[k] \ge \Gamma$. Brief threshold crossings do not accumulate, whereas sustained violations produce persistent growth in $S[k]$ until the decision level is reached. Following detection, localisation is performed by quantifying the contribution of each inverter to PCC voltage inconsistency. The per-inverter normalised voltage-consistency energy is defined as:

$$J_v^{(r)}(t) = \frac{1}{T}\int_{t-T}^{t} \left\| \frac{r_v^{(r)}(\tau)}{V_{\mathrm{nom}}} \right\|_2^2 d\tau, \tag{8}$$

with contribution score $\pi_r(t) = \dfrac{J_v^{(r)}(t)}{\sum_{\ell=1}^{R_{\mathrm{inv}}} J_v^{(\ell)}(t) + \varepsilon}$, where $\varepsilon > 0$ prevents division by zero. Larger π_r indicates stronger contribution to PCC voltage inconsistency. In discrete time, the integrals are computed using the same sliding-window sum as in Algorithm 1, yielding $J_v^{(r)}[k]$ and $\pi_r[k]$.

V. Small-Signal Stability Margin

The residual-based monitoring framework detects sustained growth in boundary voltage and current mismatches. To provide a structural interpretation, this section relates residual amplification to the small-signal stability properties of the interconnected microgrid. As the dominant eigenvalue of the linearised boundary-coupled system approaches the imaginary axis, boundary perturbations become increasingly amplified, resulting in sustained growth of the residual energy metric.

The decomposed regional model in (3) is linearised around an operating point $(x_r^\star, z_r^\star, v_b^\star, u_r^\star)$. Let $\Delta(\cdot)$ denote small deviations from this point. The linearised dynamics are:

$$\begin{bmatrix} \Delta\dot{x}_r \\ \Delta i_b^{(r)} \end{bmatrix} = \begin{bmatrix} A_r & B_{rv} & B_{ru} \\ C_r & D_{rv} & D_{ru} \end{bmatrix} \begin{bmatrix} \Delta x_r \\ \Delta v_b^{(r)} \\ \Delta u_r \end{bmatrix}, \tag{9}$$

where the matrices denote Jacobians evaluated at the operating point. Eliminating the internal state Δx_r yields a reduced boundary relation $\Delta i_b^{(r)}(s) = G_r(s)\,\Delta v_b^{(r)}(s) + H_r(s)\,\Delta u_r(s)$, where $G_r(s)$ represents the effective dynamic admittance of inverter region r at the PCC.

In the single-bus configuration of Fig. 2, all inverter boundary voltages satisfy $\Delta v_b^{(r)} = \Delta v_{\mathrm{PCC}}$. With the linearised load relation as $\Delta i_{\mathrm{load}} = Y_L(s)\Delta v_{\mathrm{PCC}}$, applying KCL yields:

$$\Big(Y_L(s) - \sum_{r=1}^{R_{\mathrm{inv}}} G_r(s)\Big)\Delta v_{\mathrm{PCC}}(s) = \sum_{r=1}^{R_{\mathrm{inv}}} H_r(s)\,\Delta u_r(s). \tag{10}$$

In the absence of external perturbations ($\Delta u_r = 0$), the natural small-signal modes (i.e., the eigenvalues of the linearised interconnected system) are determined by the roots of $\det\Big(Y_L(s) - \sum_{r=1}^{R_{\mathrm{inv}}} G_r(s)\Big) = 0$. Let $\{\lambda_i\}$ denote these eigenvalues, and define the dominant eigenvalue as $\lambda_{\max} = \arg\max_i \Re\{\lambda_i\}$. A stability margin indicator is defined as $M_\lambda(t) = -\Re\{\lambda_{\max}(t)\}$, representing the damping margin of the dominant mode. As $M_\lambda(t)$ decreases toward zero, the dominant eigenvalue approaches the imaginary axis and damping is reduced. In this regime, boundary perturbations are increasingly amplified, leading to sustained growth in the residual energy metric $\tilde{J}(t)$.

Notably, the stability margin is evaluated offline by linearising the Simulink model at representative operating points in order to interpret the relationship between residual amplification and reduced damping. However, the online monitoring framework itself relies only on measurable boundary residuals and does not require eigenvalue computation, system linearisation, or internal state reconstruction during operation, making the method suitable for real-time distributed deployment.

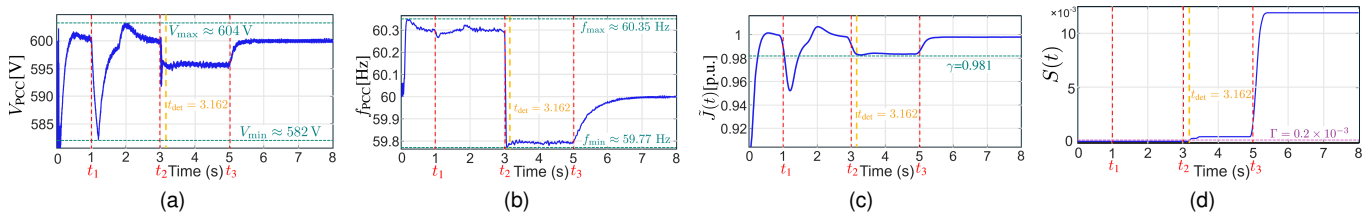

Fig. 3. Dynamic response and level-based residual monitoring: (a) PCC RMS voltage $V_{\rm PCC}$. (b) PCC frequency $f_{\rm PCC}$. (c) Normalised residual energy $\tilde{J}(t)$ and threshold γ. (d) Persistence statistic $S(t)$ and decision level Γ.

VI. Results: Detection and Instability Awareness

This section evaluates the SMD-based monitoring framework under representative operating conditions in the islanded microgrid introduced in Section II. The results assess (i) robustness to benign load disturbances, (ii) detection of droop-law modifications and supervisory adjustments, and (iii) localisation of the inverter responsible for boundary inconsistency at the PCC. The nonlinear microgrid model is implemented in MATLAB/Simulink, and monitoring follows Section IV and Algorithm 1. The residual energy $\tilde{J}(t)$ is computed using a sliding window of length T with sampling interval Δt, and baseline statistics under nominal operation determine the threshold γ and CUSUM parameters. Monitoring is activated after a dead time $T_{\rm dead}$ to suppress switching transients. Table I summarises the numerical settings and detection metrics.

A single time-domain experiment illustrates the monitoring behaviour under progressive structural changes. At t_1 = 1 s, the aggregate load is increased, producing a transient voltage dip and frequency deviation (Fig. 3(a)-(b)). This benign disturbance causes a temporary variation in the residual energy $\tilde{J}(t)$ (Fig. 3(c)), which then decays as synchronisation and proportional power sharing are restored. Accordingly, the persistence statistic $S(t)$ remains below the decision level Γ (Fig. 3(d)), indicating no sustained anomaly or instability. At t_2 = 3 s, a structural regime change is introduced by modifying the droop law, altering the effective coupling at the PCC and shifting the operating equilibrium. In contrast to the load step, this modification produces a persistent change in the residual response. The gated CUSUM statistic accumulates and crosses the decision level at $t_{\rm det} = 3.162$ s, yielding a latency of $t_{\rm det} - t_2$ = 0.162 s. A supervisory adjustment at $t_3 = 5$ s further shifts the operating point, but detection has already been declared.

At the detection instant ($t_{\rm det}$=3.162 s), the PCC voltage remains close to nominal, with $|V_{\rm PCC}(t_{\rm det}) - V_{\rm nom}| \approx 0.008$ p.u., which is significantly smaller than the global maximum deviation reported in Table I. The frequency deviates from its baseline mean $\bar{f}_0$ and exhibits an increased rate-of-change during the coupling adjustment. The detector responds to sustained structural inconsistency rather than instantaneous magnitude excursions, demonstrating its sensitivity to regime shifts in inter-inverter coupling. The sustained increase in $\tilde{J}(t)$ after the droop-law modification is consistent with the reduction in damping margin predicted by the small-signal interpretation in Section V.

TABLE I
Detection settings and dynamic response summary (60 Hz design nominal frequency).

Quantity	Value	Units
Sampling interval Δt	5×10^{-5}	s
Window length T	0.20	s
Baseline window	[0.40, 0.90]	s
Structural-change onset t_2	3.0	s
Dead time $T_{\rm dead}$	0.1	s
Threshold γ	0.981	–
Slack (CUSUM) κ	2.403×10^{-7}	–
Decision level Γ	0.2×10^{-3}	–
Baseline mean frequency $\bar{f}_0$	60.3045	Hz
Detection time $t_{\rm det}$	3.162	s
Latency $t_{\rm det} - t_2$	0.162	s
Global max $\lvert V_{\rm PCC} - V_{\rm nom}\rvert$	0.03	p.u.
Global max $\lvert f_{\rm PCC} - \bar{f}_0\rvert$	0.5345	Hz
Global max $\lvert \dot{f}_{\rm PCC}\rvert$ (50 ms filtered)	9.9865	Hz/s

Conventional magnitude-based monitoring using PCC voltage deviation alone responds primarily to instantaneous excursions caused by load disturbances. By comparison, the proposed persistence-based boundary residual metric distinguishes short transient deviations from sustained structural coupling changes, thereby reducing false alarms under benign operating events.

To visualise energy distribution across inverter regions, the centred log-asymmetry is defined as:

$$\Delta \log_{10}\big(J_v^{(r)}(t)\big) = \log_{10}\big(J_v^{(r)}(t)\big) - \frac{1}{R_{\rm inv}} \sum_{\ell=1}^{R_{\rm inv}} \log_{10}\big(J_v^{(\ell)}(t)\big). \quad (11)$$

Subtracting the regional mean removes the common-mode component and isolates inter-inverter imbalance. Fig. 4 compares the asymmetry surfaces under two operating conditions. Under a nominal load disturbance (Case 1), the asymmetry is temporary and decreases as synchronisation and power sharing are restored, indicating balanced behaviour across inverters. After the droop-law modification and supervisory adjustment (Case 2), the asymmetry shows a sustained bias along one inverter index, indicating persistent imbalance in the residual distribution. Although the overall magnitude is similar, Case 2 remains asymmetric over time, whereas Case 1 returns to near-symmetric behaviour. This suggests that structural regime changes produce sustained inter-regional imbalance rather than short-lived transient effects.

Localisation performance is quantified using the contribution scores $\pi_r(t)$. At the detection time $t_{\rm det}$, the dominant inverter index and its contribution level are defined as:

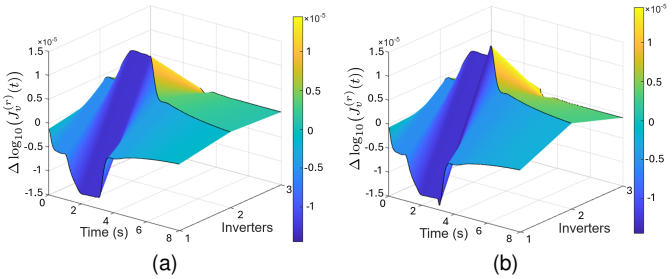

Fig. 4. Comparison of residual asymmetry surfaces: (a) Case 1: nominal load step. (b) Case 2: load, droop-law modification, and supervisory control.

$$r^\star = \arg \max_{r\in\{1,\dots,R_{\text{inv}}\}} \pi_r(t_{\text{det}}), \qquad \pi^\star = \max_{r\in\{1,\dots,R_{\text{inv}}\}} \pi_r(t_{\text{det}}). \tag{12}$$

Localisation confidence is quantified via the separation margin between the largest and second-largest contribution scores $\Delta\pi = \pi_{(1)}(t_{\text{det}}) - \pi_{(2)}(t_{\text{det}})$, where $\pi_{(1)} \geq \pi_{(2)} \geq \dots$ denote the ordered values. At the detection instant ($t_{\text{det}} = 3.162$ s), the dominant inverter is $r^\star = 1$, with $\pi^\star = 0.74$, significantly larger than the uniform value $1/R_{\text{inv}} \approx 0.33$. The separation margin is $\Delta\pi = 0.56$, indicating clear distinction between the dominant inverter and the remaining regions. These results demonstrate that the proposed framework not only detects persistent structural deviations, but also identifies the inverter most responsible for boundary inconsistency at the PCC.

Although the case study considers a three-inverter microgrid for clarity and visualisation of inter-regional residual behaviour, the computational structure is independent of system size. Each additional region contributes only local boundary measurements and residual updates. The sliding-window energy and CUSUM computations require constant-time operations per region and avoid global model reconstruction or eigenvalue analysis. The formulation therefore extends naturally to larger multi-inverter or multi-bus microgrids using the same boundary-residual construction, preserving its distributed and lightweight character.

VII. Conclusion

This paper presented a distributed monitoring framework for inverter-dominated microgrids based on SMD. By expressing the system as subsystems coupled through boundary variables, interface consistency conditions were converted into measurable residual signals. A normalised residual energy metric combined with a gated CUSUM detector enabled detection of sustained structural changes using only boundary measurements at inverter terminals and the PCC, without observer design or internal state reconstruction. Simulation results demonstrated that the method distinguishes load disturbances from droop-law modifications, detects structural changes before large voltage deviations develop, and correctly localises the dominant inverter. Following detection, the localisation signals and contribution scores can support higher-level supervisory or protection actions, including adaptive droop retuning, converter resynchronisation, load shedding, inverter isolation, or microgrid reconfiguration. The proposed framework therefore acts as an early-warning and localisation layer that provides fast structural awareness before large-scale instability propagation develops. Persistent residual growth reflects altered coupling behaviour at the PCC. The framework remains distributed, scales linearly with the number of boundary ports, and extends naturally to multi-bus microgrids.

Acknowledgment

The work is supported by the U.K. Leverhulme Trust grant RPG-2023-107 and Lancaster University EPSRC Impact Acceleration Account grant (EP/X525583/1).

References

[1] L. Fan, Z. Miao and H. Ding, "Enabling Technology for Energy Sustainability: Power Electronic Converter Control for Renewables," *IEEE Energy Sustainab. Mag.*, vol. 1, no. 2, pp. 139-153, Aug. 2025.

[2] D. B. Rathnayake et al., "Grid Forming Inverter Modeling, Control, and Applications," *IEEE Access*, vol. 9, pp. 114781-114807, 2021.

[3] Y. Gu and T. C. Green, "Power System Stability With a High Penetration of Inverter-Based Resources," *Proceedings of the IEEE*, vol. 111, no. 7, pp. 832-853, July 2023.

[4] F. N. Esfahani, N. Suri and X. Ma, "Machine Learning Forecasting and GAN-Based Scenario Control for EV Charging and PV Integration," *IECON 2025 – 51st Annual Conference of the IEEE Industrial Electronics Society*, Madrid, Spain, 2025, pp. 1-6.

[5] F. N. Esfahani, N. Suri and X. Ma, "A Two-Level Machine Learning Framework for Managing EV Charging and Renewable Energy Curtailment in Smart Grids," *2025 International Conference on Clean Electrical Power (ICCEP)*, Villasimius, Italy, 2025, pp. 568-575.

[6] R. Mittal, Z. Miao and L. Fan, "Stability Enhancement for IBRs Operating in Weak Grids Through Proper Coordination and Control," *IEEE Trans. Energy Convers.*, vol. 39, no. 3, pp. 1497-1508, Sept. 2024.

[7] X. Chen, S. Bu and I. Kocar, "Grid-Forming IBRs Under Unbalanced Grid Conditions: Challenges, Solutions, and Prospects," *IEEE Trans. Sustain. Energy*, vol. 16, no. 4, pp. 3031-3047, Oct. 2025.

[8] Q. Liu, M. Wang, M. Nick, C. Chen and X. Zhao, "Current-Limiting Control Design for Grid-Forming Capability Enhancement of IBRs Under Asymmetric Grid Disturbances," *IEEE Trans. Power Electron.*, vol. 41, no. 4, pp. 6430-6448, April 2026.

[9] H. Alduaij, Y. Weng and H. Li, "Beyond Monotonic Droop: Expanding Feasible Control Regions for Optimal Frequency Regulation," *IEEE Trans. Power Syst.*, vol. 41, no. 1, pp. 185-197, Jan. 2026.

[10] A. Pratap Yadav, M. M. Olama, A. Riza Ekti and N. M. Stenvig, "Consensus-Based Control and Optimization of Power System Inertia," *IEEE Access*, vol. 13, pp. 212150-212160, 2025.

[11] A. Joshi, A. I. Aygun, S. Kamalasadan and K. Biju, "Inverter-Angle-Induced Optimized Frequency Regulation Approach for AC-DC Microgrids Using Consensus-Based Identification," *IEEE Trans. Ind. Appl.*, vol. 58, no. 5, pp. 6780-6792, Sept.-Oct. 2022.

[12] S. S. Koduru, V. S. P. Machina, S. Madichetty and S. Mishra, "A Robust Data Driven FDI attack Detection Framework for Inverter based Microgrids," *2025 International Conference on Power Electronics Converters for Transportation and Energy Applications (PECTEA)*, Jatni, India, 2025, pp. 1-6.

[13] P. Anantarativakorn and T. Kerdphol, "Long Short-Term Memory-Based Approach for Ensuring Cyber-Security in Grid-Forming Inverters," *IEEE Access*, vol. 13, pp. 165941-165955, 2025.

[14] T. Hossen, D. Sharma and B. Mirafzal, "Smart Inverter Twin Model for Anomaly Detection," *2021 IEEE 22nd Workshop on Control and Modelling of Power Electronics (COMPEL)*, Cartagena, Colombia, 2021.

[15] X. Song et al., "Research on Performance of Real-Time Simulation Based on Inverter-Dominated Power Grid," *IEEE Access*, vol. 9, pp. 1137-1153, 2021.

[16] F. N. Esfahani, N. Suri and X. Ma, "Enhancing Cybersecurity and Resilience in Distribution Networks via Hybrid Partitioning and GAN-Driven Dynamic Reconfiguration," *IEEE Trans. Ind. Appl.*, vol. 62, no. 2, pp. 3570-3587, March-April 2026.

[17] E. De Tuglie, S. M. Iannone and F. Torelli, "A Coherency Recognition Based on Structural Decomposition Procedure," *IEEE Trans. Power Syst.*, vol. 23, no. 2, pp. 555-563, May 2008.